Article

Electrically driven long-range solid-state amorphization in ferroic In_2Se_3

https://doi.org/10.1038/s41586-024-08156-8

Received: 11 July 2023

Accepted: 4 October 2024

Published online: 6 November 2024

Check for updates

Gaurav Modi[1,4], Shubham K. Parate[2,4], Choah Kwon[3], Andrew C. Meng[1], Utkarsh Khandelwal[1], Anudeep Tullibilli[2], James Horwath[1], Peter K. Davies[1], Eric A. Stach[1], Ju Li[3], Pavan Nukala[2]✉ & Ritesh Agarwal[1]✉

Electrically induced amorphization is uncommon and has so far been realized by pulsed electrical current in only a few material systems, which are mostly based on the melt–quench process[1]. However, if the melting step can be avoided and solid-state amorphization can be realized electrically, it opens up the possibility for low-power device applications[2–5]. Here we report an energy-efficient, unconventional long-range solid-state amorphization in a new ferroic β″-phase of indium selenide nanowires through the application of a direct-current bias rather than a pulsed electrical stimulus. The complex interplay of the applied electric field perpendicular to the polarization, current flow parallel to the van der Waals layer and piezoelectric stress results in the formation of interlayer sliding defects and coupled disorder induced by in-plane polarization rotation in this layered material. On reaching a critical limit of the electrically induced disorder, the structure becomes frustrated and locally collapses into an amorphous phase[6], and this phenomenon is replicated over a much larger microscopic-length scale through acoustic jerks[7,8]. Our work uncovers previously unknown multimodal coupling mechanisms of the ferroic order in materials to the externally applied electric field, current and internally generated stress, and can be useful to design new materials and devices for low-power electronic and photonic applications.

The microscopic mechanisms driving the formation of amorphous and other disordered phases from ordered phases in materials has long perplexed scientists[9–11]. Conventionally, amorphization involves the rapid cooling of a liquid melt, bypassing thermodynamically favourable crystallization[12]. However, direct crystal–amorphous transformation without going through a melt–quench process are also known[13]. Examples of solid-state amorphization (SSA) pathways include ion irradiation[14], high-pressure treatment[15] and severe plastic deformation[16]. SSA proceeds by the addition of defects to a crystal, thereby creating a metastable crystalline phase. When disorder reaches a threshold, the crystalline phase becomes unstable and it collapses into an amorphous phase[2,6]. Although there are a few examples of amorphization in which a mechanically driven process is used, electrically driven SSA is relatively uncommon and discovering their pathways in new materials will be useful for designing energy-efficient devices[3,4].

Electrically driven SSA was reported in single-crystalline nanowires of phase-change-memory germanium–antimony–tellurium (Ge–Sb–Te) alloys in which an interplay of unique bonding hierarchy, structural distortion and large number of Ge vacancies resulted in defect-mediated amorphization[2,3]. In crystalline GeTe, polar ordering was observed. However, degenerate doping from Ge vacancies renders the system metallic, which precludes the direct coupling of polar domains with an external electric field[17–19]. Thus, in Ge–Sb–Te, carrier wind force interaction with defects and polar domains was used to construct a low-power SSA pathway. Conventional ferroelectrics are electrically insulating[20], which allows the order parameter to couple with the electric field and not with the carrier wind force. Using field-controlled frustration and disorder in ferroic systems to design low-energy SSA is an unexplored territory and requires finding materials with the right balance of ferroic nature and electrical conductivity to enable a multimode coupling to electric field and current. Polymorphs of indium selenide (In_2Se_3) provide rare materials platforms that can be both ferroic and semiconducting[21–24]. Here we explore the unusual coupling between the electric field, current, ensuing stress and structural order in a new ferroelectric β″-phase of In_2Se_3 nanowires and illustrate how it leads to an unconventional crystal–amorphous transformation. We show that the electric field and current create interlayer-sliding-induced faults and coupled in-plane polarization rotation, eventually leading to a frustrated multiconfigurational state, which is a precursor for local (nanoscopic) SSA. This process is spatially replicated over a much larger microscopic-length scale through piezoelectric stress and stress fluctuations, resulting in long-range amorphization. Our experiments shed light on the mechanisms behind a fundamentally different order–disorder transition through a multimodal coupling between ferroic and crystalline order with an external field, current and piezoelectric stress.

[1]Department of Materials Science and Engineering, University of Pennsylvania, Philadelphia, PA, USA. [2]Centre for Nanoscience and Engineering, Indian Institute of Science, Bengaluru, India. [3]Department of Materials Science and Engineering, Massachusetts Institute of Technology, Cambridge, MA, USA. [4]These authors contributed equally: Gaurav Modi, Shubham K. Parate. ✉e-mail: pnukala@iisc.ac.in; riteshag@seas.upenn.edu

Crystal structure and ferroelectricity in β″-In_2Se_3

In_2Se_3 has many polymorphs such as α, β, β′, γ, δ and κ (ref. 25), with many of them having ferroic properties. β′-In_2Se_3 is particularly interesting as it has been reported to be antiferroelectric[23], ferrielectric[26] and ferroelastic[24]. We synthesized In_2Se_3 nanowires in a new ferroelectric variant of the β′-phase (which we refer to as β″-In_2Se_3) through a catalyst-assisted vapour–liquid–solid growth mechanism[27] (Methods and Supplementary Fig. 1). The crystal structure of the as-synthesized nanowires was characterized by scanning transmission electron microscopy (STEM). Selected area electron diffraction (SAED) data show that the nanowires are single crystalline with a <11$\bar{2}$0> growth direction (Fig. 1a). In addition to the primary SAED reflections for a rhombohedral crystal, three discernible superlattice reflections along <1$\bar{1}$00> can also be seen, suggesting a superstructure formation (Supplementary Fig. 2 shows the simulated SAED) with a periodicity of $4d_{1\bar{1}00}$ (ref. 27). This is in contrast to the 7–9 superlattice reflections reported for β′-In_2Se_3 (ref. 23). Hence, depending on the nanomaterial shape and geometry, the ferroic order in β′-In_2Se_3 variants can have multiple possible configurations and many metastable states (Supplementary Note 1). High-resolution (HR) high-angle annular dark-field (HAADF) STEM imaging further shows the bright–dark contrast modulation due to superstructure formation with approximately 1.35 nm ($4d_{1\bar{1}00}$) periodicity along <1$\bar{1}$00> (Fig. 1b,e). Notably, the contrast from the lattice sites in our HRSTEM images is inverted compared with 2H β′-In_2Se_3 (refs. 23,24,26), which suggests a stacking variant of type 1T (ref. 28) (Supplementary Figs. 3 and 4). The 1T phase is rare in In_2Se_3 and has been reported only in nanowires[28]. Fast Fourier transform (FFT) of the HRSTEM image (Fig. 1b, inset) also shows three superlattice reflections. However, in some regions, extra weak spots and diffuse streaking are also observed due to some defects (dislocations) in the pristine nanowire (Supplementary Fig. 5). The atomic displacement map (Fig. 1c), in which we track the in-plane geometrical displacement of the central Se atom (darker contrast) relative to the brighter hexagonal reference lattice sites, shows that, on average, the in-plane Se displacement is approximately 15 pm and along <1$\bar{1}$00>, as opposed to the antiferroelectric or ferrielectric arrangement with polarization along <11$\bar{2}$0> in β′-In_2Se_3. Crystal symmetry analysis by convergent-beam electron diffraction shows a {11$\bar{2}$0} mirror plane (Fig. 1d and Supplementary Fig. 6) for β″-In_2Se_3 nanowires in contrast to a {1$\bar{1}$00} mirror plane for β′-In_2Se_3 (ref. 23).

Energy-dispersive X-ray spectroscopy (EDX) mapping (Fig. 1g and Supplementary Fig. 7) shows a periodic oscillation of the In/Se ratio, which we attribute to periodic In- and Se-vacancy-rich layers. The dark bands in the superstructure correspond to In-vacancy-rich regions, whereas Se-vacancy-rich regions correspond to the centre of the brighter bands, which is further confirmed by the line intensity profile of the HRSTEM image (Fig. 1e). The ordering of In vacancies has also been reported for other In-based chalcogenides such as β-In_2S_3 (refs. 29,30). Assuming nominal positive and negative charges for the Se and In vacancies, respectively, the periodically alternating vacancy-rich layers overlay an extra polarization order on the ferroelectric polarization due to Se displacements, leading to an overall ferroelectric order (Fig. 1f and Supplementary Fig. 8). Piezoresponse force microscopy (PFM) shows an off-field butterfly amplitude response[31], and a 180° phase flip (Supplementary Fig. 9), suggesting polarization switching, consistent with the presence of spontaneous ferroelectric polarization perpendicular to the growth axis (<11$\bar{2}$0>). Our DFT calculations (Methods) also validate the stability of the experimentally observed crystal structure of β″-In_2Se_3 (Fig. 1h, Supplementary Fig. 10 and Supplementary Note 2).

TEM observation of amorphization by d.c. bias

To understand the evolution of the microstructure and its relationship to its peculiar ferroelectric order on applying external electric fields, we fabricated In_2Se_3 nanowire transmission electron microscopy (TEM) devices (Methods and Supplementary Fig. 11). TEM characterization of the pristine nanowire device confirms that it has the same structure as discussed above (Fig. 2a,b). We applied direct current (d.c.) current–voltage (I–V) sweeps to this device (Fig. 2c), in which the compliance current (I_c) was slightly increased after each sweep. No changes in device resistance were observed for the first three I–V sweeps (I_c = 3.0 μA for the third sweep), but for the fourth sweep (I_c = 3.5 μA), we observed a sudden drop in current from approximately 3.1 μA to around 0.09 μA. To understand the origin of the increase in device resistance, we performed TEM imaging in which the low-magnification bright-field TEM image (Fig. 2d) clearly shows no breakage or large voids. Dark-field (DF) TEM (Fig. 2h) and HRTEM imaging (Fig. 2k) surprisingly showed that almost the entire nanowire section suspended over the trench had amorphized, accompanied by a diffuse halo contrast in the SAED data (Fig. 2e). We emphasize that the amorphization of In_2Se_3 occurred under a d.c. bias, which is different from the pulsed current required to amorphize Ge–Sb–Te nanowires[2]. Moreover, the amorphous section in the β″-In_2Se_3 nanowire spanned a large lateral width of >1 μm with a clear crystal–amorphous interface (Fig. 2h–j, blue box), and the untransformed crystalline region (Fig. 2h, green arrows) remained single crystalline and retained its superstructure (Fig. 2g,l). This is in contrast to the amorphous region with a typical width of only approximately 20 nm surrounded by a highly defective but crystalline region in Ge–Sb–Te nanowires[2,3,18,32,33]. Hence, we refer to such a crystal–amorphous transformation as 'unconventional'. EDX mapping of In/Se did not indicate any measurable differences in the stoichiometry between the crystalline and amorphous regions and as-grown nanowires (Fig. 2m and Supplementary Fig. 12), suggesting a polymorphous transition[34]. Finite-element simulations (Supplementary Fig. 13) indicate a temperature of approximately 410 K for the d.c.-biased nanowire, much less than the melting temperature of In_2Se_3 (1,163 K), ruling out the possibility of melting before amorphization (Supplementary Notes 3 and 4). Furthermore, in another device, amorphization occurred with a delay of approximately 6.2 s after applying a bias of 20 V (Extended Data Fig. 1), which reaffirms that heating (temperature) is not the sole driving force for amorphization, and a critical density of defects must be accumulated before amorphization can occur (discussed later).

Structure evolution along the amorphization pathway

Next, we applied multiple stepwise d.c. I–V sweeps (Fig. 3a) to another nanowire device to observe the structural changes occurring along the amorphization pathway. We observed that at higher voltages (>11.5 V), the I–V curve became noisy followed by a negative differential resistance (NDR) region at V > 12.75 V, followed by a permanent reduction in conductivity (Fig. 3a and Supplementary Fig. 14), suggesting the origin to be structural as opposed to electronic (Supplementary Note 5). TEM characterization of the device following NDR indeed showed evidence of numerous sliding faults, but the nanowire was still crystalline. After biasing at a d.c. electric field of approximately 10–50 kV cm^{-1} (15 V) and current density of around 10^{-2}–10^{-1} MA cm^{-2} (6–8 μA), the SAED (Fig. 3b) data show diffuse diffraction spots, along with the emergence of forbidden reflections, implying the presence of many structural imperfections (Supplementary Fig. 5). DFTEM images show unusual contrast modulations throughout the nanowire (Supplementary Fig. 15 and Fig. 3c) and that the bright–dark superstructure stripes, which were initially completely parallel along the long axis of the pristine nanowire, were distorted after electrical biasing. Application of further d.c. I–V sweeps to this nanowire resulted in sudden amorphization (Supplementary Fig. 16), suggesting its direct relationship with the observed structural changes (discussed in detail later).

HR HAADF-STEM images of another d.c.-biased nanowire device (Fig. 3d,e) further confirm this distortion, which arises because of

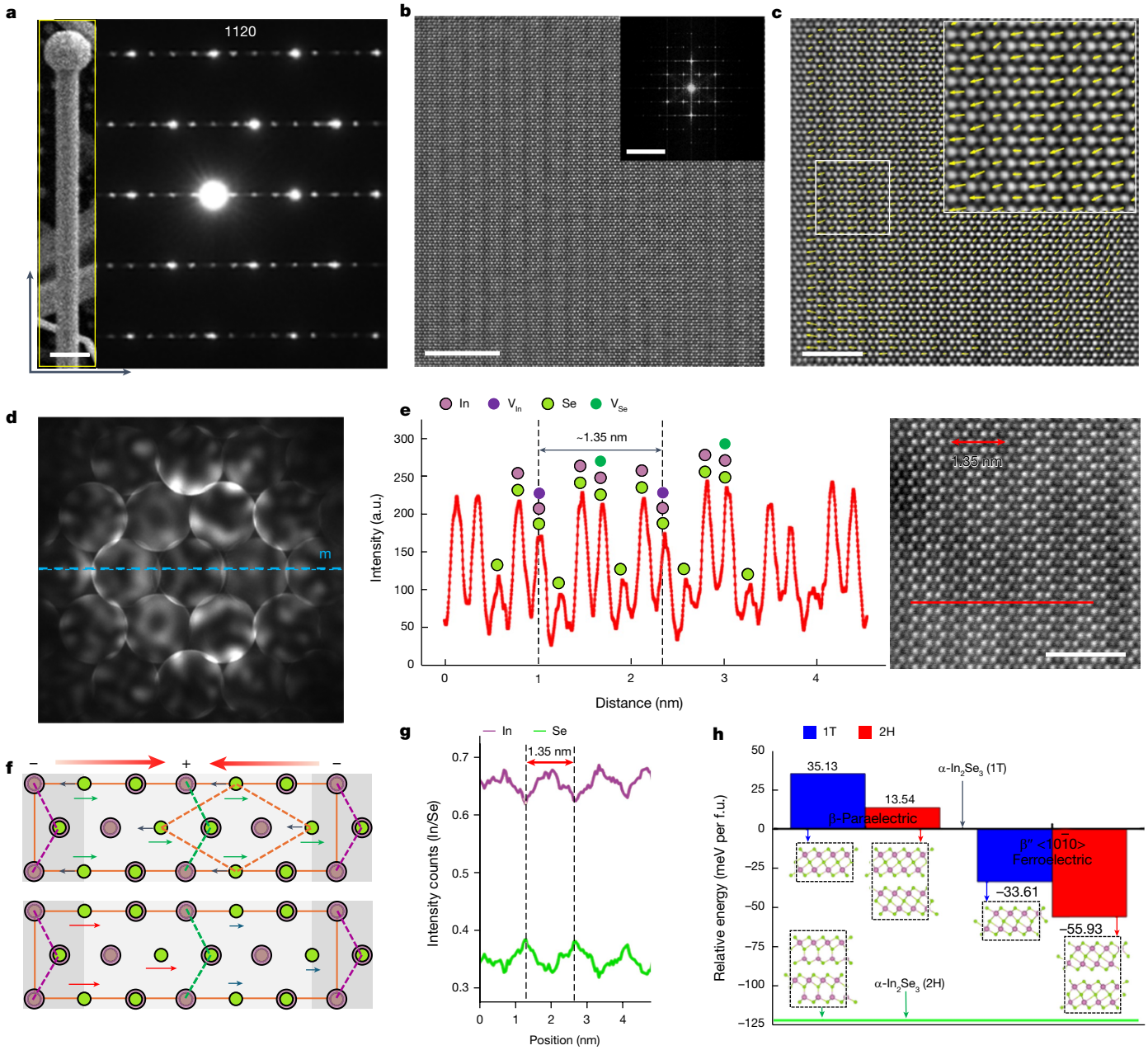

Fig. 1 | TEM characterization of as-synthesized β″-In_2Se_3 nanowires. a, Electron diffraction along the <0001> zone axis showing the presence of three superlattice reflections along one of the <1$\bar{1}$00> directions. The inset shows the scanning electron microscopy image of an In_2Se_3 nanowire with a Au–Pd catalyst at the tip. **b**, HAADF-STEM image showing superstructure modulation along <1$\bar{1}$00>. The inset shows the FFT of the STEM image. **c**, Se-atom displacement map showing that, on average, Se displacement is along <1$\bar{1}$00>, resulting in net polarization along that direction. The inset shows the magnified map of the region indicated by the white box. **d**, Convergent-beam electron diffraction data of the as-synthesized β″-In_2Se_3 nanowire, showing the presence of a {11$\bar{2}$0} mirror plane. **e**, Line intensity profile mapping along <1$\bar{1}$00> from the region indicated by the red line in the HAADF-STEM image in the inset. It reveals a 1T-stacking variant and the periodic dark regions are due to the presence of ordered In vacancies (V_{In}). V_{Se}, Se vacancies; a.u., arbitrary units. **f**, Schematic of the proposed crystal structure when viewed along <0001>, where the purple and green spheres represent the In and Se atoms, respectively. Se displacement is shown by the black arrows and polarizations are shown by the coloured arrows. The orange box indicates the unit cell of the β″-In_2Se_3 phase and the dashed orange rhombus indicates the unit cell of paraelectric β-In_2Se_3 with no Se displacements. The dashed purple and green lines pass through the lattice sites rich in In and Se vacancies, respectively. The schematic at the bottom indicates the final ferroelectric polarization arrangement due to the superposition of polarizations from vacancy layers and those due to Se displacement. **g**, EDX line profile showing the periodic variation in In and Se compositions along <1$\bar{1}$00>, implying the presence of periodic In- and Se-vacancy-rich layers. **h**, DFT calculations of the relative energies of various polymorphs of In_2Se_3 along with the schematic for the crystal structures. f.u., formula unit. Scale bars, 5 nm (**b**), 2 nm (**c** and **e**) and 10 nm^{-1} (**b**, inset).

field/current-induced interlayer sliding and the corresponding sliding faults[35]. In the next stage, at larger bias voltages (approximately 0.1 MA cm^{-2}), in which current exhibits fluctuations, eventually decreasing with increasing voltage (NDR), several sliding faults interact with each other, creating nanoscopic domains (Fig. 3f). Some of these domains can be simulated as overlapping crystals (along the $\vec{c}$ axis), with one part of the crystal sliding relative to another by different lattice and sub-lattice vectors (Fig. 3h,i and Supplementary Notes 6–8). Our calculations show that the activation barrier for nucleating one nanoscopic domain D2 by interlayer sliding is only

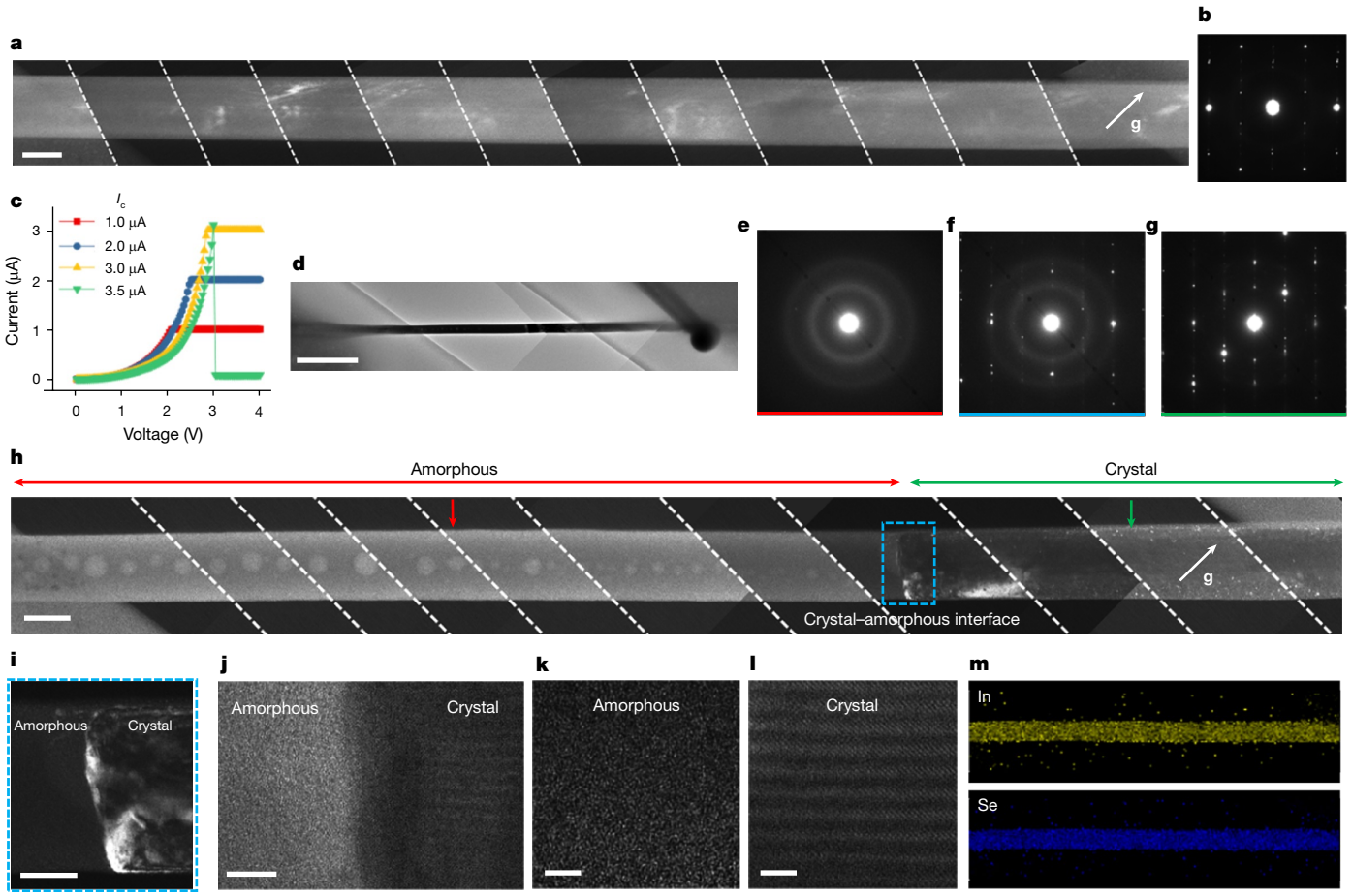

Fig. 2 | Amorphization induced by a d.c. voltage in a β″-In_2Se_3 nanowire device. a,**b**, DFTEM image (**a**) and SAED data (**b**) of a pristine nanowire device before applying any electrical stimuli. **g** indicates the reciprocal lattice vector used for DFTEM imaging. **c**, Series of 0–4 V d.c. *I*–*V* sweeps applied to the nanowires in which the compliance current was gradually increased. A sudden drop in current is seen when the current reaches approximately 3.1 μA, indicating possible amorphization. **d**, Low-magnification TEM image of the nanowire after amorphization, confirming that the drop in current was not because of breaking of the nanowire but due to amorphization. **e**–**g**, SAED data of the nanowire from the amorphous region (**e**), crystal–amorphous interface (**f**) and crystalline region (**g**) as indicated in the DFTEM image. **h**, DFTEM image of the nanowire in which the crystal–amorphous interface is indicated by the blue dashed box. The entire left side of the nanowire suspended over the trench became amorphous. Owing to the difference in material density between the amorphous and crystalline phases and a large volume of nanowire undergoing amorphization in a rather uncontrolled manner, some nanoscale voids were observed in the amorphized region. **i**,**j**, Crystal–amorphous interface is further shown in the DFTEM image (**i**) and HRTEM image (**j**). **k**,**l**, HRTEM image from the amorphous (**k**) and crystalline (**l**) regions of the nanowire. **m**, EDX mapping of the nanowires for the elements In and Se after amorphization. The dashed white lines in **a** and **h** indicate the regions in which the images were combined. Scale bars, 100 nm (**a** and **h**), 1 μm (**d**), 50 nm (**i**), 5 nm (**j**), 2 nm (**k** and **l**).

149.1 meV (Fig. 3g,h). Hence, several such nanoscopic configurations can be created with small driving forces, resulting in a free-energy landscape with multiple local minima along the reaction coordinate (Supplementary Fig. 17a). Such a high-entropy configuration is a precursor for localized SSA, as can be noted from the DFTEM image and corresponding FFT acquired from the region of intersecting defects (Fig. 4a–c).

Furthermore, spontaneous polarization will also respond to the electric field[36], positively feeding back into the creation of sliding faults through the carrier wind force. Hence, the initial <1$\bar{1}$00> polarization direction, which is a metastable phase in β″-In_2Se_3 nanowires formed during growth, can easily rotate its polarization orthogonally under the application of a d.c. bias (Fig. 3g). However, the polarization rotation is not homogeneous due to pre-existing and electrically generated inhomogeneities and defects, generating inhomogeneous piezoelectric stress[37,38]. Along with Joule-heating-assisted dipole disordering, these factors create a 'frustrated' multidomain polarization state. This state is visible from the streaky position of Se atoms in the HRSTEM image (Fig. 3e,f), with each polarization domain intertwined with the nanoscopic stacking domains (Fig. 3f).

In situ TEM observation of amorphization

To visualize the real-time microstructural evolution leading to long-range SSA because of multimodal coupling (field, stress, current and temperature), we performed in situ biasing on another device with some prior electrical history (Supplementary Fig. 18 and Supplementary Note 9) and followed its time evolution through DFTEM imaging (Fig. 4a; resolution approximately, 1 nm; **g** = [1$\bar{1}$00]) and the corresponding FFT. The FFT in the starting state captures superstructure reflections (Fig. 4b), which will be interpreted as a proxy for long-range structural order. The DFTEM image shows sliding faults (and other disorder) appearing as a diffuse halo in the FFT (Fig. 4b) with applied bias. Regions in which several faults intersect do not show any long-range order (Fig. 4c,d), indicating a localized 'nucleation' of SSA.

Supplementary Video 1 shows that small bias voltages (approximately 5 V) also create subtle dynamics to the already existing sliding defects, as can also be noted from the series of FFTs at different times (Supplementary Fig. 18). Supplementary Video 2 shows the defect dynamics on subjecting the device to *I*–*V* stressing from 15 to 25 V. In the transport behaviour, we observe current fluctuations at a bias of >20 V (Fig. 4e),

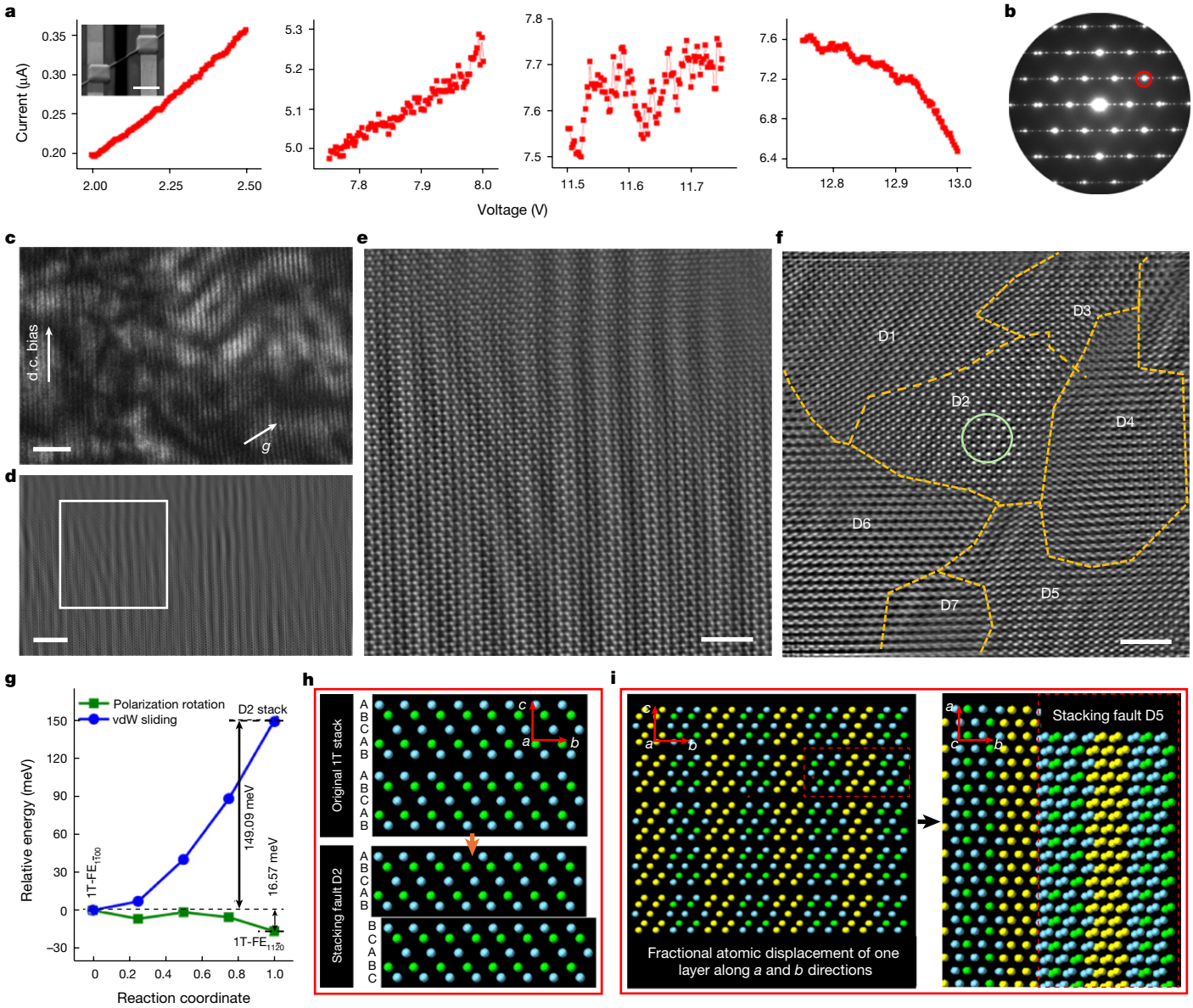

Fig. 3 | STEM analysis of a β″-In_2Se_3 nanowire device exhibiting sliding faults after applying a series of d.c. *I*–*V* sweeps before amorphization. a, *I*–*V* sweeps on the nanowire showing a change in behaviour from a positive *I*–*V* slope to noisy behaviour and finally the slope becoming negative, indicating an increase in structural disorder (the nanowire is still crystalline). The inset shows the scanning electron microscopy image of a nanowire device on a TEM chip. Scale bar, 5 μm. **b**, Electron diffraction showing the appearance of extra superlattice reflections apart from the usual three, which indicates the formation of numerous lattice defects in the nanowire. The red circled spot was used for DFTEM imaging. **c**–**e**, DFTEM (**c**), low-magnification HRSTEM (**d**) and high-magnification HRSTEM (**e**) images from a different nanowire device after multiple *I*–*V* sweeps, showing the distortion of the superstructure because of the creation of sliding faults. The superstructure contrast is enhanced first by Bragg filtering the raw HRSTEM image (Supplementary Fig. 19c) and then overlaying it on the Fourier-filtered image showing just the superstructure periodicity (Supplementary Fig. 19e). **f**, HAADF-HRSTEM image showing various nanoscopic regions (indicated by D1, D2, D3 and so on) created by interlayer-sliding-induced disorder just before amorphization. **g**, DFT-trained machine learning calculation of the activation barrier for the rotation of polarization from the <1$\bar{1}$00> to <11$\bar{2}$0> direction and for interlayer sliding along <1$\bar{1}$00>. **h**, Schematic of transformation from 1T (ABCAB ABCAB) to D2 (ABCAB BCABC) configuration through interlayer van der Waals (vdW) sliding mechanism. **i**, Results from the simulation on the steps involved in forming the nanoscopic region with stacking configuration D5. Scale bars, 10 nm (**c**), 5 nm (**d**), 2 nm (**e**) and 2 nm (**f**).

similar to other devices (Fig. 3a and Supplementary Figs. 14 and 22a). The DFTEM video shows that concomitant with the current fluctuations (or local field fluctuations), the strain field also fluctuates in a correlated manner (snapshots in Fig. 4f–h) obtained at the corresponding points (labelled f, g and h) on the *I*–*t* curve (Fig. 4e). The perfect synchronization of field fluctuations (Fig. 4e) and acoustic jerks (Fig. 4f–h) is evidence of piezoelectricity, and these jerks themselves resemble Barkhausen noise characteristic of disordered ferroelectrics emanating from intersecting dynamic domain boundaries[7,8,39]. Conversely, the observation of such noise stands as the evidence of polarization rotation and interaction among sliding faults and domains in our system[40] (Supplementary Note 9).

Supplementary Video 3 captures the amorphization process, which immediately follows the current fluctuations and the NDR regime (Fig. 4i). On following the FFT of the DFTEM image, we see that the FFT, to start with, shows streaky patterns (Fig. 4j) of what were sharper modulation vectors (Fig. 4b), clearly suggesting an increase in disorder in the superstructure arising from In- and Se-vacancy ordering,

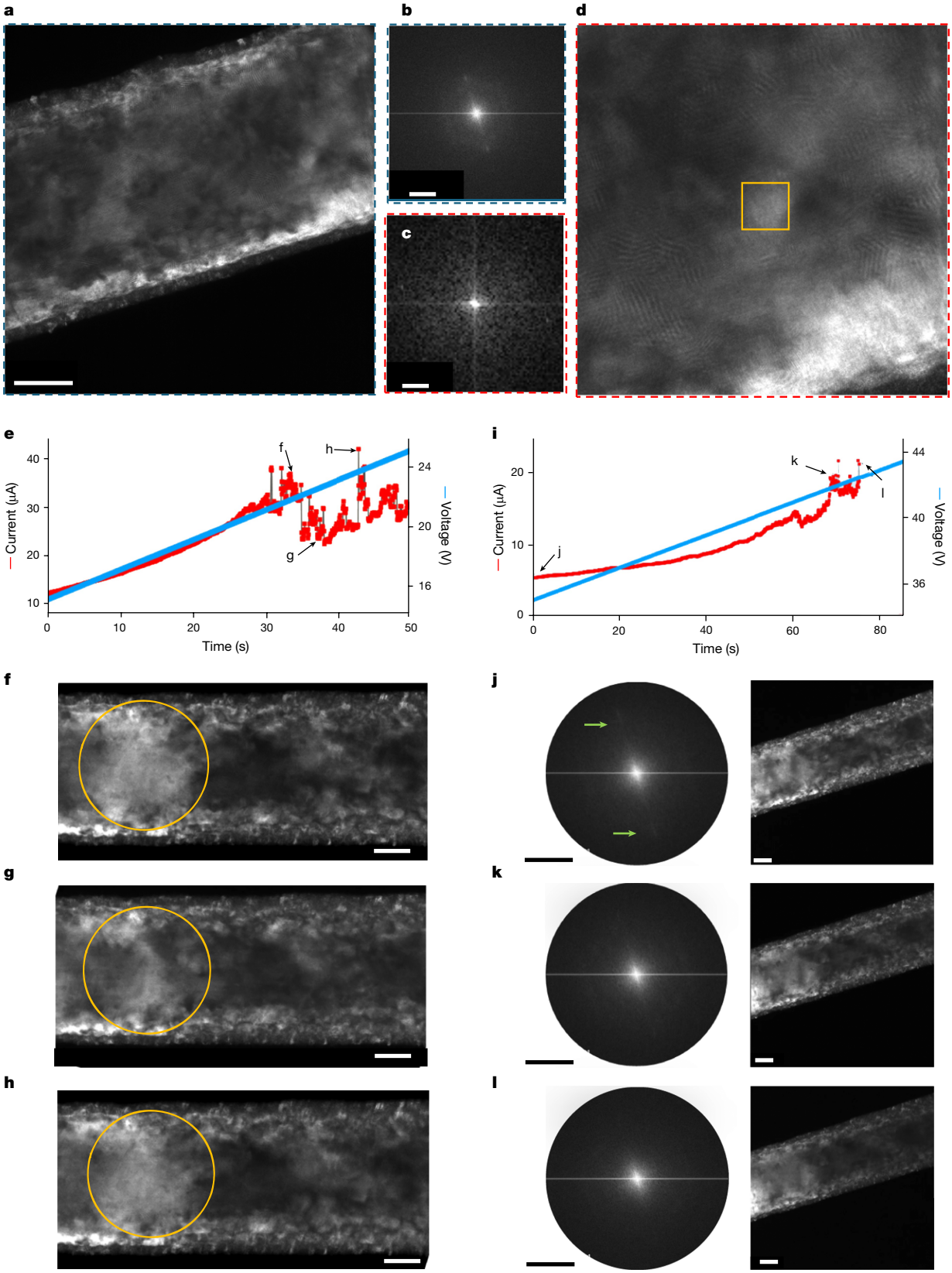

Fig. 4 | In situ biasing DFTEM imaging of β″-In_2Se_3 nanowire device and observation of amorphization. a,**b**, DFTEM image of the initial state of another nanowire device (**a**) and the corresponding FFT (**b**) showing superstructure reflections and a diffuse halo corresponding to sliding faults and other defects or disorder. **c**,**d**, FFT (**c**) of a region obtained from the intersection of several sliding faults marked in the DFTEM image in **d**, showing a local loss of order. **e**–**h**, *V*–*t* and *I*–*t* characteristics (**e**) of the device, and snapshots of the DFTEM images (**f**–**h**) from Supplementary Video 2 capturing strain-field fluctuations corresponding to the points marked in **e**. **i**, *V*–*t* and *I*–*t* characteristics of the device, and snapshots of DFTEM images and their FFTs (**j**–**l**) from Supplementary Video 3 at the points marked in **i**. The FFTs capture evolution from streaky patterns corresponding to disorder in superstructure reflections (**j**) to a complete loss of intensity in the streaks on SSA (**k** and **l**). Scale bars, 50 nm (**a** and **f**–**h**), 50 nm (**j**–**l**, right).

perpendicular to the nanowire. At the point at which larger fluctuations in current originate (Fig. 4i, point labelled k), corresponding to large strain-field fluctuations in both amplitude and spatial extent (DFTEM image shown in Fig. 4k), these streaky patterns in FFT further lose intensity, becoming more diffuse (Fig. 4k). Eventually, the current reduces (Fig. 4i), with the FFT of the DFTEM image showing only diffuse scattering (Fig. 4l) corresponding to long-range SSA.

Discussion

On the basis of our observations, we propose the following model for amorphization: electric field and carrier wind force provide a driving force for polarization rotation (domain-boundary motion) and sliding fault formation, initially in a local region (nanoscale). The ensuing piezoelectric stress due to polarization rotation creates similar defects over a longer range, dictated by the length scale of mechanical stress. As more sliding faults are created, they interact and cause strain-field fluctuations, which further create (replicate) more sliding faults, leading to much smaller domains (and more domain boundaries). The interaction of many sliding faults and domain boundaries locally causes the loss of long-range order (nanometre-length scale; Fig. 4c), nucleating SSA. These regions are replicated spatially (micrometre-length scales) through long-range strain fields, and this can be construed as multiple nucleation events of the amorphous phase. All these amorphous nuclei locally grow due to acoustic jerks, further disrupting the local crystalline order. Electrically, a collapse of current occurs once the percolative crystalline pathways are cut off completely by the growing amorphous nuclei (Supplementary Note 9). Such long-range electrically induced SSA has not been reported in any other system, which highlights the interplay of unique structure, piezoelectricity and ferroelectricity in β″-In_2Se_3 and the coupling of order parameter to external fields, essential for converting field fluctuations into long-range strain fluctuations.

In conclusion, we uncovered a unique long-range SSA process in ferroelectric β″-In_2Se_3 nanowires on applying a d.c. bias, facilitated by a complex interplay of electric field, current, piezoelectric stress, acoustic jerks and Joule heating. β″-In_2Se_3 is a model material system in which the synergistic confluence of various material properties (layered, semiconducting, ferroelectric and piezoelectric) results in an unconventional amorphization process. We believe that similar studies on other semiconducting ferroic materials can unlock other metastable phase transformations, which holds the potential for designing new materials and devices.

Online content

Any methods, additional references, Nature Portfolio reporting summaries, source data, extended data, supplementary information, acknowledgements, peer review information; details of author contributions and competing interests; and statements of data and code availability are available at https://doi.org/10.1038/s41586-024-08156-8.

1. Wong, H. S. P. et al. Phase change memory. *Proc. IEEE* **98**, 2201–2227 (2010).
2. Nam, S. W. et al. Electrical wind force-driven and dislocation-templated amorphization in phase-change nanowires. *Science* **336**, 1561–1566 (2012).
3. Nukala, P., Lin, C. C., Composto, R. & Agarwal, R. Ultralow-power switching via defect engineering in germanium telluride phase-change memory devices. *Nat. Commun.* **7**, 10482 (2016).
4. Lee, S. H., Jung, Y. & Agarwal, R. Highly scalable non-volatile and ultra-low-power phase-change nanowire memory. *Nat. Nanotechnol.* **2**, 626–630 (2007).
5. Jung, Y., Nam, S. W. & Agarwal, R. High-resolution transmission electron microscopy study of electrically-driven reversible phase change in $Ge_2Sb_2Te_5$ nanowires. *Nano Lett.* **11**, 1364–1368 (2011).
6. Fecht, H. J. Defect-induced melting and solid-state amorphization. *Nature* **356**, 133–135 (1992).
7. Zapperi, S., Cizeau, P., Durin, G. & Stanley, H. E. Dynamics of a ferromagnetic domain wall: avalanches, depinning transition, and the Barkhausen effect. *Phys. Rev. B* **58**, 6353–6366 (1998).
8. Casals, B., Nataf, G. F. & Salje, E. K. H. Avalanche criticality during ferroelectric/ ferroelastic switching. *Nat. Commun.* **12**, 345 (2021).
9. Biroli, G. Disordered solids: in search of the perfect glass. *Nat. Phys.* **10**, 555–556 (2014).
10. Berthier, L. & Biroli, G. Theoretical perspective on the glass transition and amorphous materials. *Rev. Mod. Phys.* **83**, 587–645 (2011).
11. Russo, J., Romano, F. & Tanaka, H. Glass forming ability in systems with competing orderings. *Phys. Rev.* **8**, 021040 (2018).
12. Klement, W., Willens, R. H. & Duwez, P. Non-crystalline structure in solidified gold–silicon alloys. *Nature* **187**, 869–870 (1960).
13. Zhang, L. et al. Amorphous martensite in β-Ti alloys. *Nat. Commun.* **9**, 506 (2018).
14. Rehn, L. E., Okamoto, P. R., Pearson, J., Bhadra, R. & Grimsditch, M. Solid-state amorphization of Zr_3Al: evidence of an elastic instability and first-order phase transformation. *Phys. Rev. Lett.* **59**, 2987–2990 (1987).
15. Bridges, F. et al. Local vibrations and negative thermal expansion in ZrW_2O_8. *Science* **280**, 886–890 (1998).
16. He, Y. et al. In situ observation of shear-driven amorphization in silicon crystals. *Nat. Nanotechnol.* **11**, 866–871 (2016).
17. Shportko, K. et al. Resonant bonding in crystalline phase-change materials. *Nat. Mater.* **7**, 653–658 (2008).
18. Nukala, P. et al. Inverting polar domains via electrical pulsing in metallic germanium telluride. *Nat. Commun.* **8**, 15033 (2017).
19. Edwards, A. H. et al. Electronic structure of intrinsic defects in crystalline germanium telluride. *Phys. Rev. B* **73**, 045210 (2006).
20. Lines, M. E. & Glass, A. M. *Principles and Applications of Ferroelectrics and Related Materials* (Oxford Univ. Press, 2001).
21. Ding, W. et al. Prediction of intrinsic two-dimensional ferroelectrics in In_2Se_3 and other III_2-VI_3 van der Waals materials. *Nat. Commun.* **8**, 14956 (2017).
22. Xiao, J. et al. Intrinsic two-dimensional ferroelectricity with dipole locking. *Phys. Rev. Lett.* **120**, 227601 (2018).
23. Xu, C. et al. Two-dimensional antiferroelectricity in nanostripe-ordered In_2Se_3. *Phys. Rev. Lett.* **125**, 47601 (2020).
24. Xu, C. et al. Two-dimensional ferroelasticity in van der Waals β′-In_2Se_3. *Nat. Commun.* **12**, 3665 (2021).
25. Zhang, Z. et al. Atomic visualization and switching of ferroelectric order in β-In_2Se_3 films at the single layer limit. *Adv. Mater.* **34**, 2106951 (2022).
26. Wang, L. et al. In-plane ferrielectric order in van der Waals β′-In_2Se_3. *ACS Nano* **18**, 809–818 (2024).
27. Peng, H., Schoen, D. T., Meister, S., Zhang, X. F. & Cui, Y. Synthesis and phase transformation of In_2Se_3 and $CuInSe_2$ nanowires. *J. Am. Chem. Soc.* **129**, 34–35 (2007).
28. Liu, L. et al. Atomically resolving polymorphs and crystal structures of In_2Se_3. *Chem. Mater.* **31**, 10143–10149 (2019).
29. Van Landuyt, J., Hatwell, H. & Amelinckx, S. The domain structure of β-In_2S_3 'single crystals' due to the ordering of indium vacancies. *Mater. Res. Bull.* **3**, 519–528 (1968).
30. Van Landuyt, J. & Amelinckx, S. Antiphase boundaries and twins associated with ordering of indium vacancies in β-In_2S_3. *Phys. Status Solidi B Basic Solid State Phys.* **31**, 589–600 (1969).
31. Chen, P. J. & Montgomery, S. T. A macroscopic theory for the existence of the hysteresis and butterfly loops in ferroelectricity. *Ferroelectrics* **23**, 199–207 (1980).
32. Modi, G., Stach, E. A. & Agarwal, R. Low-power switching through disorder and carrier localization in bismuth-doped germanium telluride phase change memory nanowires. *ACS Nano* **14**, 2162–2171 (2020).
33. Modi, G. et al. Controlled self-assembly of nanoscale superstructures in phase-change Ge–Sb–Te nanowires. *Nano Lett.* **24**, 5799–5807 (2024).
34. Yan, Z. H., Klassen, T., Michaelsen, C., Oehring, M. & Bormann, R. Inverse melting in the Ti-Cr system. *Phys. Rev. B* **47**, 8520–8527 (1993).
35. Li, W., Qian, X. & Li, J. Phase transitions in 2D materials. *Nat. Rev. Mater.* **6**, 829–846 (2021).
36. Matzen, S. et al. Super switching and control of in-plane ferroelectric nanodomains in strained thin films. *Nat. Commun.* **5**, 4415 (2014).
37. Gao, P. et al. Revealing the role of defects in ferroelectric switching with atomic resolution. *Nat. Commun.* **2**, 591 (2011).
38. Fu, H. & Cohen, R. E. Polarization rotation mechanism for ultrahigh electromechanical response. *Nature* **403**, 281–283 (2000).
39. Salje, E. K. H., Wang, X., Ding, X. & Scott, J. F. Ultrafast switching in avalanche-driven ferroelectrics by supersonic kink movements. *Adv. Funct. Mater.* **27**, 1700367 (2017).
40. Sui, F. et al. Atomic-level polarization reversal in sliding ferroelectric semiconductors. *Nat. Commun.* **15**, 3799 (2024).

Methods

Synthesis of In_2Se_3 nanowires

In_2Se_3 nanowires in the β″-phase (Supplementary Fig. 1) were grown by a catalyst-assisted vapour–liquid–solid mechanism. An approximately 5-nm-thick Au–Pd catalyst layer was sputtered on a silicon substrate and was used for nanowire growth. The Au–Pd film breaks down into catalyst nanoparticles on heating in the furnace. About 10 mg of In_2Se_3 powder (Sigma-Aldrich) was placed at the centre of a 2.54-cm tube furnace (Lindberg/Blue M), whereas the silicon substrate was placed approximately 10 cm downstream from the centre of the furnace. Before starting nanowire growth, the furnace was flushed multiple times with argon gas until a pressure of approximately 30 mtorr was reached to remove any residual oxygen. After that, the argon flow rate was set to 120 s.c.c.m. and the tube pressure was stabilized at approximately 50 torr. The furnace temperature was set to 700 °C and nanowire growth was carried out for 5 h, after which the furnace was gradually cooled down to room temperature.

Device fabrication

Electrical devices were fabricated on circular TEM grids (diameter, 3.05 mm) from Ted Pella with a 0.25 mm × 0.25 mm silicon nitride (SiN_x) membrane in the centre (Supplementary Fig. 11). Electron-beam lithography was used to pattern the electrodes on the TEM grids. First, the TEM grid was spin coated with two layers (approximately 50 nm each) of PMMA 950 A2 resist with resist baking at 180 °C after each spin coat. A pre-defined array of electrodes was patterned by electron-beam lithography, followed by the physical vapour deposition of approximately 10 nm Ti and around 30 nm Au. A TESCAN S8000X focused ion beam (FIB) was used to pattern trenches (width, approximately 1–2 μm; length, around 60 μm) in between the metal electrodes to enable HRTEM imaging. Following that, nanowires were dry transferred by gently tapping the patterned TEM grids on the nanowire growth substrate. Final electrical connections were established by depositing platinum through FIB at the point of contact of the nanowire with the patterned electron-beam lithography electrodes. The time and area of FIB exposure were carefully controlled to avoid any material damage from the ion beam. The open and lateral device geometry of the nanowires and their single-crystalline structure offer a favourable material system to image the evolution of the microstructure with high spatial resolution, as well as simultaneously minimizing the effects of pre-existing grain and domain boundaries on the structural dynamics.

Electrical characterization of devices

All the electrical measurements were performed in a two-probe configuration on a Lake Shore TTPX cryogenic probe station. The d.c. *I*–*V* sweeps were applied using a Keithley 2602 source meter. For monitoring the evolution of current with time as the d.c. voltage is held constant, we used an electrical setup shown in Supplementary Fig. 21. A constant d.c. bias was applied to the nanowire device connected in series with a standard 1 MΩ resistor through a Keithley 2635B source measure unit. Current was indirectly measured as the voltage drop across the standard resistor using a 500 MHz Tektronix DPO3052 digital oscilloscope with a 1 MΩ impedance. Hence, the actual current through the nanowire (Extended Data Fig. 1) is twice that indicated in Extended Data Fig. 1, but for the sake of proportionality, the actual magnitude of current is not as important.

HAADF-STEM imaging and Se displacement mapping

The imaging was carried out on an aberration-corrected Titan Themis instrument, which was operated at 300 kV. A probe angle of 24 mrad was used for imaging the nanowires in the STEM mode with a HAADF collection angle of 48–200 mrad. The obtained HR images were further processed to get enhanced contrast of dislocations by first Bragg filtering the raw image (Supplementary Fig. 19a–c) and overlaying this image with the inverse FFT image (Supplementary Fig. 19d,e) obtained by masking only the spots given by band periodicity to obtain the final dislocation-contrast-enhanced images (Supplementary Fig. 19f). For mapping the Se displacement vector, we first found the geometric centre of each hexagon and then subtracted it from the central Se positions by using atom finding and refining algorithms from Atomap[41]. In this way, Se displacements from their geometric centres were mapped.

PFM switching

In_2Se_3 nanowires were transferred to Si substrates sputtered with gold and clamped at the ends by depositing platinum in an FIB Helios 5 UX DualBeam instrument. PFM spectroscopy measurements were carried out on AFM Asylum Research MFP-3D Origin+ in the dual-amplitude resonance tracking mode. The nanowires were mapped using the tapping mode followed by Dual AC Resonance Tracking PFM spectroscopy measurements by moving the tip to the points of interest. Voltage pulses were applied with amplitude varying from 0 to V_{max}, V_{max} to $-V_{max}$ and $-V_{max}$ to 0 (sawtooth envelope). The amplitude and phase of the piezoresponse is measured when every pulse is on (field-on response) and after a short delay, once the pulse is turned off (field-off response). The remnant loops (field off) of amplitude (Supplementary Fig. 9a) and phase (Supplementary Fig. 9b) show that the displacements are consistent with the polarization-switching behaviour.

In situ TEM measurements

The in situ TEM heating experiment (Supplementary Video 4) was performed on a JEOL F200 STEM instrument in the TEM/diffraction mode. The nanowires were dry transferred on a Hummingbird Scientific heating chip (Supplementary Fig. 23a) by gently tapping the TEM chip on the nanowire growth substrate. A specialized single-tilt heating/biasing TEM holder from Hummingbird Scientific was used to monitor the structural changes during the in situ heating experiment. Temperature calibration was received from the manufacturer to achieve controlled heating based on the resistance measurements, for which the current was applied through an externally connected power supply.

In situ TEM electrical biasing experiments (Supplementary Videos 1–3) were performed on a Thermo Fisher Titan Themis 300 instrument, in the DFTEM and diffraction modes. Nanowires were transferred onto the microelectromechanical-systems-based biasing chip (DENSsolutions), and contacts were made to the metal pads on the chip through FIB. The chip was then loaded onto a lightning biasing holder (DENSsolutions), which was externally connected to a Keithley parameter analyser (Model 4200) for electrical measurements. The DFTEM images/videos were simultaneously captured as the devices were electrically biased in two modes: (1) constant voltage as a function of time and (2) linear ramp of voltage as a function of time. Sampling time for both electrical data and DFTEM images was set to be the same. The application of bias results in small mechanical motion of the nanowire, which is used to synchronize the electrical stimulus with the DFTEM images.

DFT calculations

The thermodynamic stability and phase transformation between In_2Se_3 polymorphs were calculated using spin-polarized DFT and the preferred potential[42,43] machine learning potential implemented in the Matlantis program, respectively. The DFT calculations were performed with the projector augmented wave[44] method and the Perdew–Burke–Ernzerhof[45] exchange–correlation functional of the generalized gradient approximation using the Vienna ab initio simulation package[46,47]. Monkhorst–Pack grids of 10 × 6 × 10 *k*-points, energy convergence criteria of 10^{-5} eV and force convergence criteria of 0.02 eV $Å^{-1}$ were applied. Our DFT calculations assume a temperature of 0 K, but vibrational free-energy contribution at room temperature and higher temperatures can stabilize the initial structure. Moreover, it is possible to observe thermodynamically metastable configurations in experiments, depending on the external mechanical, thermal and electrical driving

conditions, which can drive the system out of equilibrium. The activation barriers for phase transformation between In_2Se_3 polymorphs were obtained using the climbing image nudged elastic band[48] method with a convergence criterion of 0.1 eV $Å^{-1}$. The DFT-trained machine learning potential is a universal interatomic potential[43], and is accurate enough to describe the saddle energy barriers. It should be noted that for the sake of computational simplicity, we did not consider the In and Se vacancies in our structures for DFT calculations (Supplementary Note 10).

Data availability

The datasets generated and analysed during the current study are included with the Article or available from the corresponding authors upon reasonable request. Source data are provided with this paper.

41. Nord, M., Vullum, P. E., MacLaren, I., Tybell, T. & Holmestad, R. Atomap: a new software tool for the automated analysis of atomic resolution images using two-dimensional Gaussian fitting. *Adv. Struct. Chem. Imaging* **3**, 9 (2017).
42. Takamoto, S. et al. Towards universal neural network potential for material discovery applicable to arbitrary combination of 45 elements. *Nat. Commun.* **131**, 2991 (2022).
43. Takamoto, S., Okanohara, D., Li, Q. J. & Li, J. Towards universal neural network interatomic potential. *J. Mater.* **9**, 447–454 (2023).
44. Kresse, G. & Joubert, D. From ultrasoft pseudopotentials to the projector augmented-wave method. *Phys. Rev. B* **59**, 1758 (1999).
45. Perdew, J. P., Burke, K. & Ernzerhof, M. Generalized gradient approximation made simple. *Phys. Rev. Lett.* **77**, 3865 (1996).
46. Kresse, G. & Hafner, J. Ab initio molecular dynamics for liquid metals. *Phys. Rev. B* **47**, 558 (1993).
47. Kresse, G. & Furthmüller, J. Efficient iterative schemes for ab initio total-energy calculations using a plane-wave basis set. *Phys. Rev. B* **54**, 11169 (1996).
48. Henkelman, G., Uberuaga, B. P. & Jónsson, H. A climbing image nudged elastic band method for finding saddle points and minimum energy paths. *J. Chem. Phys.* **113**, 9901–9904 (2000).

Acknowledgements This work was supported by the ONR-MURI (grant no. N00014-17-1-2661) and partially supported by the US NSF (FuSe; no. 2328743), US Air Force Office of Scientific Research (award no. FA9550-23-1-0189) and ANRF-SERB:CRG/2022/003506, Government of India. Support from NSF-MRSEC/DMR-2309043 seed grant is also acknowledged. P.N. acknowledges Indian Institute of Science (IISc) start-up seed grant and Infosys young researcher award. Electron microscopy and PFM measurements were carried out at the Advanced Facility for Microscopy and Microanalysis and the Micro Nano Characterization Facility in IISc. Device fabrication work and electron microscopy was conducted at the Singh Center for Nanotechnology, which is supported by the NSF National Nanotechnology Coordinated Infrastructure Program under grant no. NNCI-2025608 and through the University of Pennsylvania Materials Research Science and Engineering Center (MRSEC) (grant no. DMR-1720530). P.N. and S.K.P. are grateful for the support received from V. Dey in setting up a robust biasing system for the in situ TEM experiments.

Author contributions G.M. and R.A. conceptualized the project, and along with P.N. and S.K.P., designed the experiments and analysed the data. G.M. performed the nanowire synthesis, device fabrication, electrical characterization, in situ and ex situ TEM experiments, device modelling and finite element analysis. S.K.P. and P.N. performed the ex situ HAADF-STEM imaging, and in situ DFTEM biasing experiments. C.K. and J.L. carried out the DFT calculations. A.C.M. helped with the four-dimensional STEM polarization mapping. U.K. helped with the nanowire synthesis. A.T. and P.N. performed the PFM measurements and analysis. J.H. assisted with the in situ TEM heating setup. E.A.S. provided suggestions for the TEM characterization. P.K.D. helped with the structure interpretation and data analysis. G.M. and R.A. wrote the manuscript with inputs from S.K.P. and P.N. All authors discussed the results and commented on the final manuscript.

Competing interests E.A.S. is an equity holder in Hummingbird Scientific. The other authors declare no competing interests.

Additional information

Supplementary information The online version contains supplementary material available at https://doi.org/10.1038/s41586-024-08156-8.

Correspondence and requests for materials should be addressed to Pavan Nukala or Ritesh Agarwal.

Peer review information *Nature* thanks Junwei Zhang and the other, anonymous, reviewer(s) for their contribution to the peer review of this work. Peer reviewer reports are available.

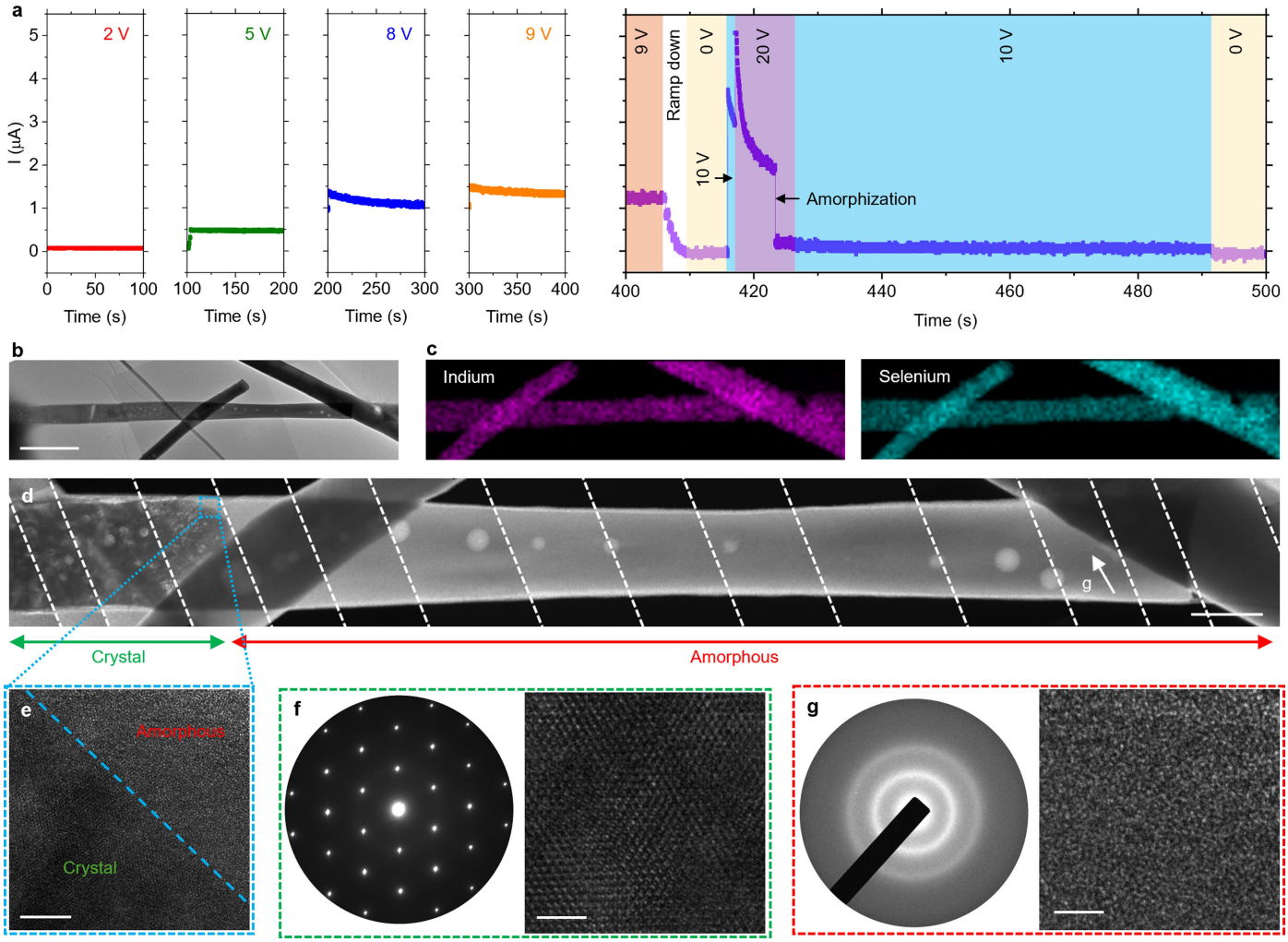

Extended Data Fig. 1 | TEM characterization of amorphized β″-In_2Se_3 nanowire device upon application of d.c. voltage. (**a**) Evolution of current in the nanowire device with time when the device is held at different fixed d.c. voltages. Amorphization occurs at 20 V and is preceded by a rapid decrease in current with time. (**b**) Low magnification TEM image of the nanowire device after amorphization. (**c**) EDX elemental mapping of indium and selenium in the amorphized region of the nanowire. (**d**) DF-TEM image of the nanowire after amorphization. The contrast from the crystal-amorphous interface can be seen at the left side of the nanowire, where a part of the interface is shown in the HR-TEM image in (**e**). Electron diffraction and HR-TEM image from the (**f**) paraelectric crystalline phase and (**g**) amorphous regions of the nanowire device. The dashed white lines in (d) indicate the regions where the images were combined. Scale bars: (b) 1 μm, (d) 200 nm, (e) 5 nm, (f) and (g) 2 nm.